

A FAST 3D IMAGING TECHNIQUE FOR NEAR-FIELD CIRCULAR SAR PROCESSING

W. Yan^{1, *}, J.-D. Xu^{1, 2}, G. Wei¹, L. Fu¹, and H.-B. He¹

¹School of Electronic and Information, Northwestern Polytechnical University, Xi'an, Shaanxi 710129, China

²Science and Technology on Space Microwave Laboratory, Xi'an, Shaanxi 710100, China

Abstract—A fast method for circular SAR three-dimensional imaging system by near-field elevation scanning is proposed in this paper. It is based on cylindrical spectrum theory which exploits the Fourier decomposition of the targets distribution instead of point by point imaging in earlier works. The proposed method sets up the relationship between the target image and the scattering field in spatial frequency domain. This leads to overcome the problem of computational inefficiency which was observed previously in projection-slice theorem. The near-field scattering is firstly analyzed by relating the return signal to the near-field focus function. The near-field focus function is then transformed to spatial frequency domain and evaluated by the method of stationary phase. Finally, the imaging result is given by three-dimensional inverse Fourier transformation from spatial frequency domain of targets. The proposed method is validated by the simulation results of distributed targets. In addition, experimental validation was also achieved in microwave chamber at X-band with targets placed on the turntable.

1. INTRODUCTION

SAR imaging technique which can be used in target scattering diagnostics and recognition has been developed for many years. The object is illuminated by a wide bandwidth electromagnetic wave at different angle from transmitting antenna, and then the scattered field is measured by receiving antenna. The spatial resolution of SAR

Received 17 May 2012, Accepted 20 June 2012, Scheduled 24 June 2012

* Corresponding author: Wei Yan (yanwei_nwpu@163.com).

system depends on the shape and dimensions of the volume occupied in the spatial frequency space [1].

In circular synthetic aperture radar (CSAR) mode, the target is illuminated by radar over a circular path. The advantage of CSAR imaging is that it can achieve two-dimensional sub-wavelength resolution image by wide-angle collection. CSAR has been widely used in automatic target recognition (ATR) system [2, 3], detection of targets in the foliage or under the ground [4, 5], detection of concealed objects in airport security systems [6], and so on.

CSAR imaging algorithm is different from traditional SAR system. The scattered data is collected over 360 degree, and it can not be focused very well by classical algorithms, such as, range Doppler (RD) algorithm [7], chirp scaling (CS) algorithm [8], and range migration algorithm (RMA) [9, 10].

One method for CSAR imaging is to divide the 360 degree circular path into small arc segments, and then utilize the reconstruction algorithm for the linear SAR system with slant correction [11]. However, the computation is inefficient and the numerous interpolation and motion compensation errors may alter the subtle phase information in a target's signature, which is crucial for detecting man-made metallic structures.

Another algorithm which was based on the Fourier analysis for CSAR was presented in [12]. It first obtains an expression for the spatial Fourier transformation of slant Green's function. Then, the generalized Parseval's theorem is used for fast computation in spatial frequency domain. Finally, the target function in the spatial domain is obtained by the inverse spatial Fourier transform of the data in spatial frequency domain. But it involves the pseudo-inversion of system kernel matrix which is unstable.

CSAR can be used for three dimensional imaging, which is known as [13]. It only uses one circular path to extract the height information of targets. The sensitivity of the algorithm in the altitude domain depends on the target's support region in the frequency domain. The height resolution for this system is limited by the volume occupation in spatial frequency domain.

One way to improve height resolution is by adding another aperture in height direction [14, 15, 19]. It uses two-dimensional CSAR image which is formed from the data collected at two complete circular apertures from different incident angles for interferometry. Although, it employs a two-frequency method to avoid phase unwrapping, the robustness of the two-frequency method is not very well.

Another way to improve the height resolution is by adding multi-pass in height direction. The SAR data is collected on multiple

complete circular apertures at different elevation angles. For this system, the three-dimensional version of the projection-slice theorem is used to obtain the image [16, 17]. However, it must be measured at uniform elevation angles intervals, which is hardly satisfied in actual environment. It also needs to be imaged point-by-point, leading to time-consuming computation. Another algorithm which is the multiplication with the cylinder focusing function and coherent summation over the measured frequency ranges is presented [18]. However, it is only validated by simulation model, and it is based on the consideration that backscattering angles of the model in azimuth is fixed.

In this paper, an imaging algorithm for three dimensional target reconstruction with multiple-pass CSAR observations is proposed. The main difference between the proposed method and the transitional method is that it employs the Fourier analysis not only in polar format of targets, but also in height domain. The computation is fast because it involves the fast Fourier transformation in spatial frequency domain. Firstly, the scattering field of targets is expressed through near field Green's function. Secondly, the height information is separated out of Green's function by using method of stationary phase (MSP). Thirdly, the circular spectrum theory is used to obtain the two dimensional targets image in the ground plane. Finally, the three dimensional targets is calculated by performing three-dimensional inverse FFT.

The structure of the paper is organized as follows. Section 2 presents the CSAR scanning geometry, signal model, the formulation of the proposed algorithm. Section 3 gives the procedure of the proposed method in details. Sections 4 and 5 assesses the performance of this algorithm by means of numerical simulation and experimental results. Finally, the conclusions of this paper are provided in Section 6.

2. SYSTEM MODEL

In CSAR system, radar is moving along a circular path to illuminate the targets. This is equivalent to the targets rotating on the turntable whereas the radar remains fixed. The geometry of a turntable system is illustrated in Figure 1. A stepped frequency signal is transmitted from an antenna, located at the horizontal distance R from the centre of the turntable, providing an isotropic irradiation to the targets. The antennas are moving from down to up around a base line, which is H higher than the turntable plane. The reflected signals are received by a similar adjacent antenna which forms a quasi-monostatic system. The targets with reflection coefficient $\psi(x, y, z)$ in Cartesian coordinates (x, y, z) are placed on a low reflectivity support in the

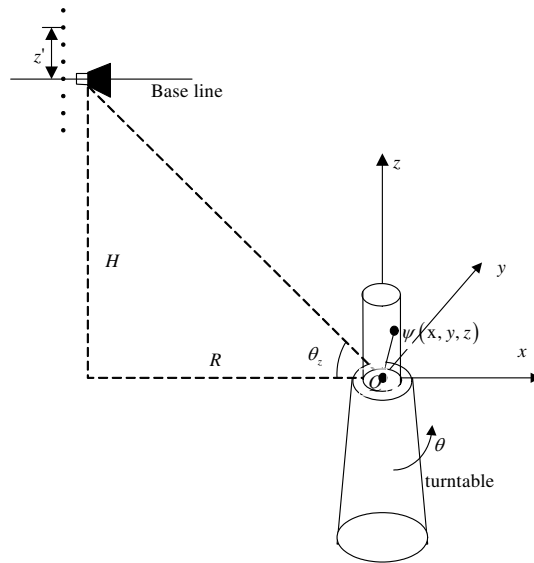


Figure 1. System model.

centre of turntable, which can rotate around the plane $x-y$. The rotated angle θ stands for the instantaneous position of the turntable. The instantaneous position between the targets and the antenna is d . The slant angle between the direction from antenna at base line to the centre of the turntable O and x axis is θ_z .

2.1. Near-field Scattering

Considering that the antenna is located in the near-field region of the objects, and the amplitude attenuation of the scattering field is negligible compared to the phase contribution. The scattering electric field of targets in the near-field can be expressed as

$$E_s(f, \theta, z') = \int_{-\infty}^{\infty} \int_{-\infty}^{\infty} \int_{-\infty}^{\infty} \psi(x, y, z) G(x, y, z; f, \theta, z') dx dy dz \quad (1)$$

where, $G(x, y, z; f, \theta, z')$ is near field focus function, which is given by $G(x, y, z; f, \theta, z') = e^{-jk \times 2d}$. Here, the wave-number is defined as $k = 2\pi f/c$ and the distance from antenna to the targets is $d = \sqrt{(x - R \cos \theta)^2 + (y - R \sin \theta)^2 + (z - z' - H)^2}$. As the position of targets (x, y, z) can be expressed as (ρ, ϕ, z) in cylindrical coordinates,

and the distance d can also be given as

$$d = \left| \vec{R} - \vec{\rho} \right| = \sqrt{R^2 + \rho^2 + 2R\rho \cos(\phi - \theta) + (z - z' - H)^2} \quad (2)$$

By noting that (1) resembles a Fourier integral, the estimate of the reflectivity image can be obtained by using an integral resembling its inverse transform, i.e.,

$$\psi(x, y, z) = \int_{-\infty}^{\infty} \int_{-\infty}^{\infty} \int_{-\infty}^{\infty} E_s(f, \theta, z') e^{j2kd} df d\theta dz' \quad (3)$$

To calculate the integral in (3), let

$$\begin{aligned} E_s(f, \theta, z) &= \int_{-\infty}^{\infty} E_s(f, \theta, z' + H) e^{j2kd} dz' \\ &= \int_{-\infty}^{\infty} E_s(f, \theta, z' + H) e^{j2k\sqrt{R^2 + \rho^2 + 2R\rho \cos(\phi - \theta) + (z - z' - H)^2}} dz' \end{aligned} \quad (4)$$

Then, Equation (3) can be expressed as

$$\psi(x, y, z) = \int_{-\infty}^{\infty} \int_{-\infty}^{\infty} E_s(f, \theta, z) df d\theta \quad (5)$$

2.2. Fourier Analysis in Spatial Frequency Domain

The calculation of formula (4) can be achieved by the one dimensional convolution in the z' domain, as

$$E_s(f, \theta, z) = E_s(f, \theta, z + H) * e^{j2k\sqrt{R^2 + \rho^2 + 2R\rho \cos(\phi - \theta) + z^2}} \quad (6)$$

The convolution in the elevation domain can be computed in the Fourier domain as a complex product if the following Fourier Transform (FT) is known

$$E(f, \theta, k_z) = \int_{-\infty}^{\infty} e^{j2k\sqrt{R^2 + \rho^2 + 2R\rho \cos(\phi - \theta) + z^2}} e^{-jk_z z} dz \quad (7)$$

$$FFT[E_s(f, \theta, z + H)] = E_s(f, \theta, k_z) \times e^{jk_z H}$$

where, $E_s(f, \theta, k_z)$ is the Fourier transformation of the return signal $E_s(f, \theta, z)$ in the elevation domain z .

Subsequently, Equation (6) can be defined as

$$E_s(f, \theta, z) = \int_{-\infty}^{\infty} E_s(f, \theta, k_z) E(k_z) e^{jk_z(z+H)} dk_z \tag{8}$$

The Equation (7) can be solved by MSP, as

$$E(f, \theta, k_z) \approx e^{jk_\rho \sqrt{R^2 + \rho^2 + 2R\rho \cos(\phi - \theta)}} \tag{9}$$

Here,

$$k_\rho = \sqrt{4k^2 - k_z^2} \tag{10}$$

Note that, in (10), k_ρ must be real and therefore the region in the wavenumber domain where the asymptotic expansion of the MSP is valid reduces to

$$k_z^2 \leq 4k^2 \tag{11}$$

The field modes which satisfy this inequality are the so-called propagating modes, whereas those which do not propagate are the evanescent modes. The amplitude of the evanescent modes is affected by an exponential factor which rapidly vanishes with an increasing distance to the aperture.

So, (8) can be expressed as

$$E_s(f, \theta, z) = \int_{-\infty}^{\infty} E_s(f, \theta, k_z) e^{jk_\rho \sqrt{R^2 + \rho^2 + 2R\rho \cos(\phi - \theta)}} e^{jk_z(z+H)} dk_z \tag{12}$$

Here, z is independent of ρ and ϕ , then Equation (3) can be written as

$$\begin{aligned} &\psi(\rho, \phi, z) \\ &= \int_{-\infty}^{\infty} \int_{-\infty}^{\infty} \int_{-\infty}^{\infty} E_s(f, \theta, k_z) e^{jk_\rho \sqrt{R^2 + \rho^2 + 2R\rho \cos(\phi - \theta)}} e^{jk_z(z+H)} df d\theta dk_z \\ &= \int_{-\infty}^{\infty} \left[\int_{-\infty}^{\infty} \int_{-\infty}^{\infty} E_s(f, \theta, k_z) e^{jk_\rho \sqrt{R^2 + \rho^2 + 2R\rho \cos(\phi - \theta)}} df d\theta \right] e^{jk_z(z+H)} dk_z \end{aligned} \tag{13}$$

Let

$$\psi(\rho, \phi, k_z) = \int_{-\infty}^{\infty} \int_{-\infty}^{\infty} E_s(f, \theta, k_z) e^{jk_\rho \sqrt{R^2 + \rho^2 + 2R\rho \cos(\phi - \theta)}} df d\theta \tag{14}$$

Then Equation (13) can be defined as

$$\psi(\rho, \phi, z) = \int_{-\infty}^{\infty} \psi(\rho, \phi, k_z) e^{jk_z(z+H)} dk_z \tag{15}$$

Equation (14) is a two dimensional summarizations which introduces the computational inefficiency. A practical method is by transforming the spatial variable ρ to spatial spectrum variable k'_ρ and using the FFT.

Hence, Equation (14) can be calculated by [2]

$$\psi(k_\rho, \phi, k_z) = 2.81 \int_{-\infty}^{\infty} \int_{-\infty}^{\infty} E_s(f, \theta, k_z) e^{jk_\rho R[1 - \frac{1}{2} \tan^2(\frac{\theta - \phi}{2})]} df d\theta \quad (16)$$

2.3. Reconstruction of Image from Spatial Frequency Domain

By substituting (14) into (15), following equation is obtained

$$\begin{aligned} & \psi(k_\rho, \phi, z) \\ = & 2.81 \int_{-\infty}^{\infty} \int_{-\infty}^{\infty} \int_{-\infty}^{\infty} E_s(f, \theta, k_z) e^{jk_\rho R[1 - \frac{1}{2} \tan^2(\frac{\theta - \phi}{2})]} e^{jk_z(z+H)} df d\theta dk_z \quad (17) \end{aligned}$$

To reconstruct the image in rectangular Plane Coordinate System, $\psi(k_x, k_y, z)$ can be interpolated by $\psi(k_\rho, \phi, z)$, where $k_x = k_\rho \sin \phi$ and $k_y = k_\rho \cos \phi$. After doing 2D inverse FFT in spatial frequency domain (k_x, k_y) , the distribution of targets $\psi(x, y, z)$ can be reconstructed. The difference between Equations (17) and (3) is that the relationship in (17) shows set-up in spatial frequency domain by using MSP. The calculation in (3) is three-dimensional summation for each point, whereas the calculation in (17) is three dimensional summation for all points.

3. RECONSTRUCTION PROCEDURE

This section deals with the practical implementation of the near-field CSAR 3D imaging algorithm. The whole procedure to reconstruct a 3D reflectivity image of targets is described as follows:

Step 1: Perform the Inverse coherent summation to $E_s(f, \theta, z')$ with respect to z' ;

Step 2: Perform the one dimensional FFT to $E_s(f, \theta, z)$ in z domain to obtain the $E_s(f, \theta, k_z)$;

Step 3: Calculate the coherent summation to transform $E_s(f, \theta, k_z)$ to $\psi(k_\rho, \phi, k_z)$;

Step 4: Performing the two dimensional interpolation to obtain $\psi(k_x, k_y, k_z)$ from $\psi(k_\rho, \phi, k_z)$;

Step 5: Performing the three dimensional inverse FFT to get $\psi(x, y, z)$.

4. SIMULATION RESULTS

In this section, the performance of the proposed fast near-field imaging method is implemented with cylindrical spectrum approach. This approach is illustrated with comparison to the near-field projection-slice method. The projection-slice method was first used in the medical imaging, and later introduced to extract the target shape information from circular path data in the reference [16, 17]. It first divides the image zone into $N \times N \times N$ grid points, and then calculates the amplitude and phase for each point.

The frequency range for the proposed model is $f = 8 \sim 12$ GHz with 401 frequency steps, the angular aperture is $\theta = 0^\circ$ to 360° with 1 degree angular step. The near-field distance R is 5 m and the height H from the base line to turntable plane is 5 m as shown in Figure 1. The antennas were set to move for a total length of 0.8 m along z axis with 0.02 m step-intervals. The targets geometry with same reflectivity 0 dBsm is shown in Figure 2(a). The far-field is defined as $2D^2/\lambda$. The targets dimension D is about 0.85 m, so the far-field is 57.8 m. The near field distance is within 10% of far field requirement. The forward solver for synthetic data without noise is based on integrating the contribution of each scatterer which can be found in the reference [4, 10].

The three dimensional imaging result obtained via proposed method is shown in Figure 2(b). It is given as the 3 dB isosurface of the targets amplitude. The shape of the result agrees well with the original target model. The target in the original point which is focused very well is a little bigger than the other targets. The slice at $z = 0$ is shown in Figure 2(c), in which the targets is just at the centre of screen. The slice at $z = -0.3$ is shown in Figure 2(d), from which the reconstructed image agrees well with the theoretical model. The computation time is 115 seconds, whereas the projection-slice method needs 382 minutes. The reason is that the proposed method obtains the image from spatial frequency domain by three-dimensional FFT; however, the projection-slice method achieved the image through point-by-point technique.

5. EXPERIMENTAL RESULTS

In order to provide empirical validation to the proposed theoretical model, the experiment was also performed in microwave chamber with dimension $7 \text{ m} \times 4 \text{ m} \times 3 \text{ m}$. The step frequency signal is generated

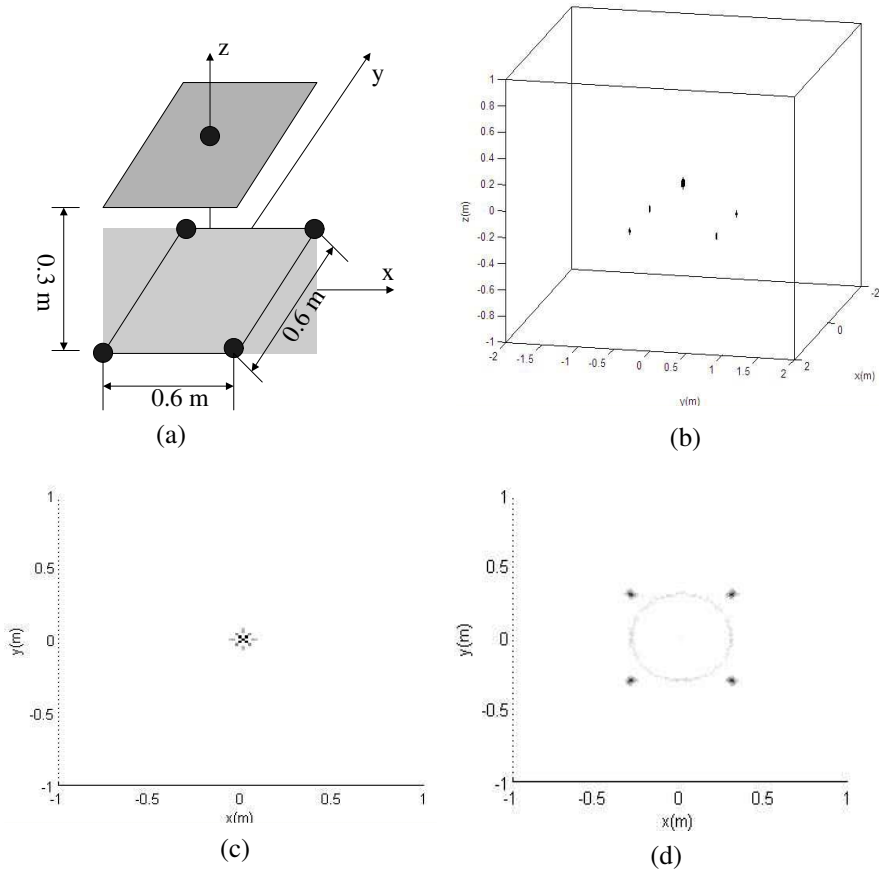


Figure 2. Simulation results. (a) Simulation model. (b) Image result of target. (c) Slice at $z = 0$ m. (d) Slice at $z = -0.3$ m.

by an Agilent Vector Network Analyzer 8363A. The received signal is also captured by Vector Network Analyzer but with different ports. The transmitting antenna and receiving antenna are standard horn antennas which can work from 1 GHz to 40 GHz. In order to collect scattering data in the experiment, the transmitting and receiving antennas are placed on a support, which can move along elevating domain.

The measurement data is obtained with the rotation of the turntable. The frequency sample is 801 from 8 GHz to 12 GHz. The angular sample is 721 with the total rotated angle 360 degree. The elevation was 0.3 m in total with 0.05 m interval steps. The distance between the center of support and the antenna is about 0.85 m, and the

altitude difference from the baseline of antenna to the turntable plane is 0.4 m. According to the far-field requirements, this distance should be over 12.8 m. Clearly, the target is in the near field zone, which is only with 10% of far-field criterion. The transmitting and receiving antennas were placed very near compared to the measured distance, therefore it forms a quasi-monostatic system.

Experimental Model-1: Targets fabricated in two layers are placed on a low scattering reflection support, as shown in Figure 3(b). The lower layer consists of four metallic spheres with radius 5 cm each, and is placed on the turntable plane, as shown in Figure 3(a). The upper layer, which is about 0.15 m higher than the lower layer, includes a similar metallic sphere with same radius placed in the center of the plane, as shown in Figure 3(c). The radius of foam support is about 0.3 meter, and it can rotate at 0.1 degree angular intervals.

The imaging result of proposed method is shown in Figure 3(d), which agrees well with the actual theoretical model. The slice at $z = -0.1$ m, and the slice at $z = 0.05$ m are shown in Figure 3(e) and Figure 3(f), respectively. In Figure 3(f), the image result not only reflects the four spheres at turntable plane, but also reflects the other sphere on the top layer which is unfocused. This shows that our proposed method is suitable for simple imagery configuration with targets of similar size and simple distribution.

Experimental Model-2: Further validation to the proposed algorithm is provided through another complex targets arrangement which was also measured in the microwave chamber. The targets are embedded in 3 layers including 9 metallic spheres with different radii. The lower layer is made up of 4 spheres with radius 5 cm each, as shown in Figure 4(a). The middle layer, which is about 0.1 m higher than the lower layer, consists of 1 sphere with radius 3 cm, as shown in Figure 4(a). The upper layer, which is about 0.15 m higher than the low layer, comprised of 4 spheres with radius 4 cm each, as shown in Figure 4(b). The three-dimensional image result is shown in Figure 4(c), which reflects the information of targets very well. The slice at $z = -0.1$ m is shown in Figure 4(d), in which the position of targets is close to the actual targets. The slice at $z = 0$ m is shown in Figure 4(e), in which the position of targets is the same to one sphere in the centre. The slice at $z = 0.1$ m is shown in Figure 4(f), in which the position of targets agree well with the four sphere in the model. In Figure 4(f), the image result not only include the information in upper layer, but also include the information from low layer which is unfocused in $z = 0.1$ m.

The experimental results in this sub-section further demonstrated that our proposed method has the potential to address more

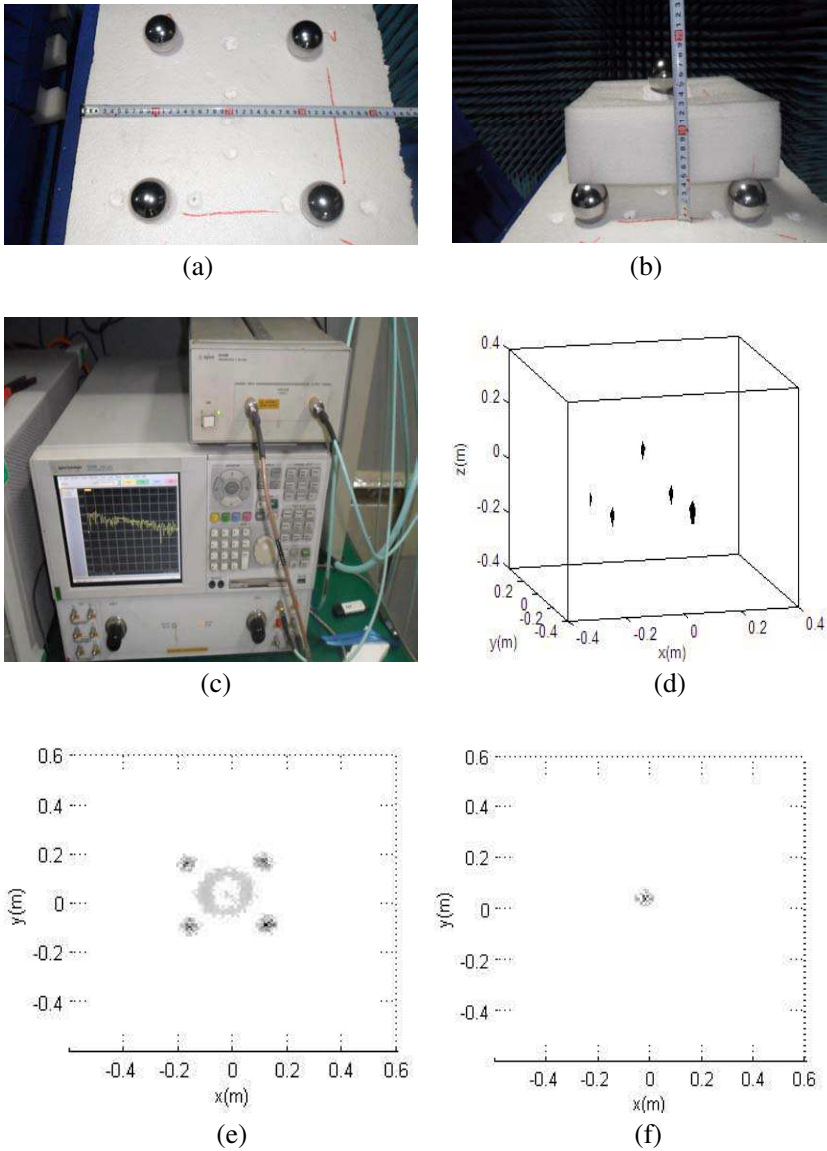


Figure 3. Experimental model and results. (a) Targets on the lower layer. (b) Target model in real space. (c) The experiment setup. (d) The image result of targets. (e) Image result at slice $z = -0.1$ m. (f) image result at slice $z = 0.05$ m.

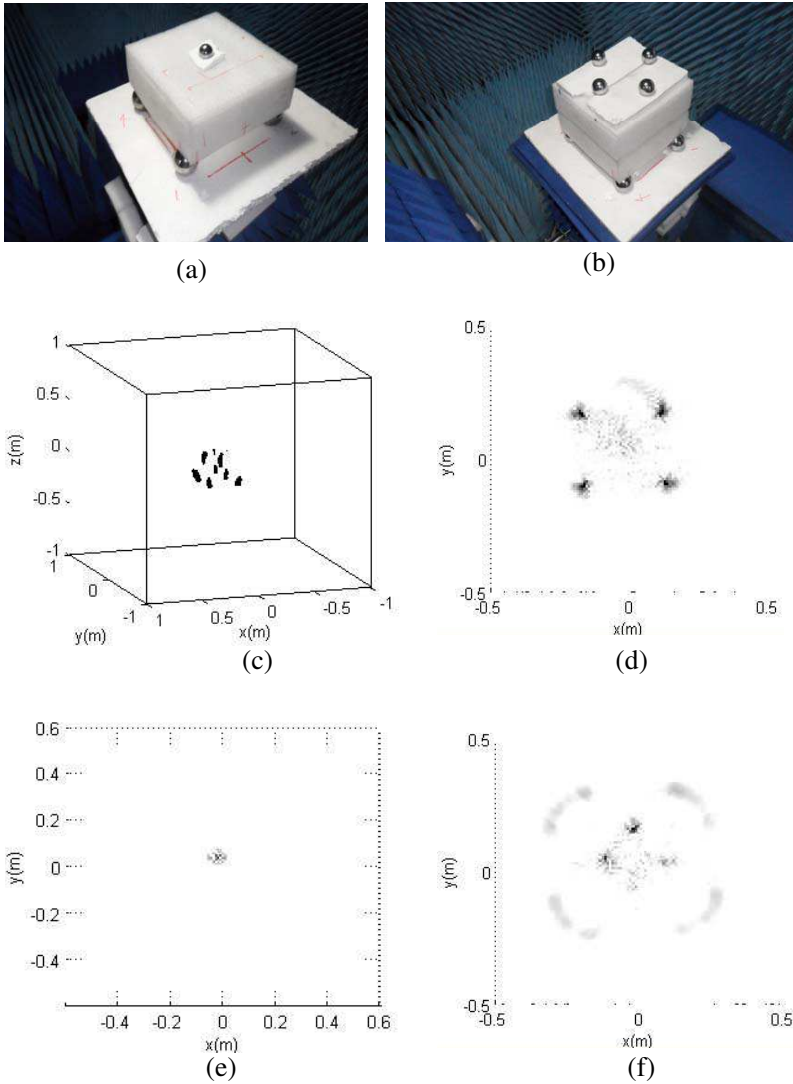


Figure 4. Experimental model and results. (a) The middle layer of targets. (b) The up layer of targets. (c) 3D result image of targets. (d) Slice at $z = -0.1$ m. (e) Slice at $z = 0$ m. (f) Slice at $z = -0.1$ m.

complicated target arrangement at multiple levels. However, further study is needed to elucidate the focus effect of the targets in complex arrangement.

6. CONCLUSION

In this paper, a fast three-dimensional imaging method for near-field circular SAR system is proposed. It is accomplished by introducing Fourier decomposition of the targets focus function in spatial frequency domain. The proposed method sets up the relationship between the target distribution and the scattering field in spatial frequency domain by the method of stationary phase. It overcomes the problem of computational inefficiency observed by back-projection method which is achieved via point by point imaging. The validation for the proposed method is achieved through simulation and also by the experimental result in microwave chamber. These results show that the proposed method has good performance and it can reconstruct the three-dimensional information of targets. Also, the computational efficiency has been improved compared to the previously used projection-slice theorem in literature. It can be used in three-dimensional automatic target recognition system in microwave chamber.

ACKNOWLEDGMENT

The authors would like to thank the anonymous reviewers for providing a number of important comments and suggestions. This work is supported by the National Key Laboratory Foundation of China (Grant No. 9140C530303110C5304) and by the National Natural Science Foundation of China (Grant No. 61102018).

REFERENCES

1. Soumekh, M., *Synthetic Aperture Radar Signal Processing with MATLAB Algorithms*, Wiley, New York, 1999.
2. Yan, W., J.-D. Xu, N.-J. Li, and W.-X. Tan, "A novel fast near-field electromagnetic imaging method for full rotation problem," *Progress In Electromagnetics Research*, Vol. 120, 387–401, 2011.
3. Solimene, R., A. Brancaccio, R. D. Napoli, and R. Pierri, "3D sliced tomographic inverse scattering experimental results," *Progress In Electromagnetics Research*, Vol. 105, 1–13, 2010.
4. Fortuny, J., "Efficient algorithms for three-dimensional near-field synthetic aperture radar imaging," Ph.D. Thesis, University of Karlsruhe, 2001.
5. Mohammadpoor, M., R. S. A. Raja Abdullah, A. Ismail, and A. F. Abas, "A circular synthetic aperture radar for on-the-

- ground object detection,” *Progress In Electromagnetics Research*, Vol. 122, 269–292, 2012.
6. Tan, W.-X., Y.-P. Wang, W. Hong, Y.-R. Wu, N.-J. Li, C.-F. Hu, and L.-X. Zhang, “Circular SAR experiment for human body imaging,” *1st Asian and Pacific Conference on Synthetic Aperture Radar*, 2007.
 7. Chan, Y. K. and V. C. Koo, “An introduction to synthetic aperture radar (SAR),” *Progress In Electromagnetics Research B*, Vol. 2, 27–60, 2008.
 8. Moreira, A., J. Mittermayer, and R. Scheiber, “Extended chirp scaling algorithm for air- and spaceborne SAR data processing in stripmap and ScanSAR imaging modes,” *IEEE Transactions on Geoscience and Remote Sensing*, Vol. 34, No. 5, 1123–1136, 1996.
 9. Guo, D. M., H. P. Xu, and J. W. Li, “Extended wavenumber domain algorithm for highly squinted sliding spotlight SAR data processing,” *Progress In Electromagnetics Research*, Vol. 114, 17–32, 2011.
 10. Lopez-Sanchez, J. M. and J. Fortuny-Guasch, “3-D Radar imaging using range migration techniques,” *IEEE Transactions on Antennas and Propagation*, Vol. 48, No. 5, 728–737, 2000.
 11. Li, Y. and D. Zhu, “The geometric-distortion correction algorithm for circular-scanning SAR imaging,” *IEEE Geoscience and Remote Sensing Letters*, Vol. 7, No. 2, 376–380, 2010.
 12. Soumekh, M., “Reconnaissance with slant plane circular SAR imaging,” *IEEE Transactions on Image Processing*, Vol. 5, No. 8, 1252–1265, 1996.
 13. Bryant, M. L., L. L. Gostin, and M. Soumekh, “3-D E-CSAR imaging of a T-72 tank and synthesis of its SAR reconstructions,” *IEEE Transactions on Aerospace and Electronic Systems*, Vol. 39, No. 1, 211–227, 2003.
 14. Lin, Y., W. Hong, W. Tan, and Y. Wu, “Interferometric circular SAR method for three-dimensional imaging,” *IEEE Geoscience and Remote Sensing Letters*, Vol. 8, No. 6, 1026–1030, 2011.
 15. Yu, L. J. and Y. H. Zhang, “A 3D target imaging algorithm based on two-pass circular SAR observations,” *Progress In Electromagnetics Research*, Vol. 122, 341–360, 2012.
 16. Ertin, E., R. L. Moses, and P. C. Lee, “Interferometric methods for 3-D target reconstruction with multi-pass circular SAR,” *2008 7th European Conference on Synthetic Aperture Radar (EUSAR)*, 1–4, 2008.
 17. Knaell, K. K. and G. P. Cardillo, “Radar tomography for the

- generation of three-dimensional images,” *IEEE Proceedings on Radar, Sonar and Navigation*, Vol. 142, No. 2, 54–60, 1995.
18. Tan, W. X., W. Hong, Y. P. Wang, and Y. R. Wu, “A novel spherical-wave three-dimensional imaging algorithm for microwave cylindrical scanning geometries,” *Progress In Electromagnetics Research*, Vol. 111, 43–70, 2011.
 19. Dallinger, A., S. Bertl, S. Schelkshorn, and J. Detlefsen, “SAR techniques for the imaging of humans,” *Sixth European Conference on Synthetic Aperture Radar (EUSAR2006)*, Dresden, Germany, May 16–18, 2006.